A Radon diffraction theorem for plane wave ultrasound imaging

Please check the document version of this publication:

• A submitted manuscript is the version of the article upon submission and before peer-review. There can be important differences between the submitted version and the official published version of record. People interested in the research are advised to contact the author for the final version of the publication, or visit the DOI to the publisher's website.
• The final author version and the galley proof are versions of the publication after peer review.
• The final published version features the final layout of the paper including the volume, issue and page numbers.

[Link to publication](#)

A Radon diffraction theorem for plane wave ultrasound imaging

Hans-Martin Schwab and Richard Lopata

ARTICLES YOU MAY BE INTERESTED IN

JASA
THE JOURNAL OF THE
ACOUSTICAL SOCIETY OF AMERICA

CALL FOR PAPERS

Special Issue: Fish Bioacoustics:
Hearing and Sound Communication

A Radon diffraction theorem for plane wave ultrasound imaging

Hans-Martin Schwab[a]) 🆔 and Richard Lopata 🆔

Department for Biomedical Engineering, Eindhoven University of Technology, Eindhoven 5612AZ, Netherlands

ABSTRACT:

The rising demand on high frame rate ultrasound imaging applications necessitates the development of fast algorithms for plane wave image reconstruction. We introduce a new class of plane wave reconstructions that relies on a relation between receive data and image data in the Radon domain. This relation is derived for arbitrary dimensions and validated on multiple two-dimensional plane wave data sets. We further present a mathematical relation between conventional delay-and-sum and Fourier domain reconstruction methods and the method proposed. Our analysis shows that they all rely on the same physical model with slight variations in certain filtering steps and, therefore, the new Radon domain reconstruction yields similar results as other methods in terms of image quality. However, we show that our method offers a huge potential to improve computation time by reducing the number of applied projections and to improve image quality by introducing nonlinear operations in the Radon domain, e.g., for edge enhancement. As the Radon transform retains both angular and temporal information, the relation also provides new insights on the fundamentals of plane wave imaging that can be leveraged for optimizing acquisition schemes or for developing novel compounding strategies in the future. © 2023 Author(s). All article content, except where otherwise noted, is licensed under a Creative Commons Attribution (CC BY) license (http://creativecommons.org/licenses/by/4.0/). https://doi.org/10.1121/10.0017245

I. INTRODUCTION

High frame rate ultrasound imaging, also known as ultrafast ultrasound imaging, allows for the acquisition of several thousand frames per second and has therefore significantly broadened the range of applications for ultrasound diagnostics. High frame rate acquisitions enable novel imaging modes, especially in fields where fast processes are imaged, such as encountered in elastography or flow imaging.[1] For many applications, plane wave ultrasound imaging with linear arrays has been shown to be a suitable approach, providing a simple trade-off between the number of transmissions and image quality.[2] Plane wave acquisitions allow for very high acquisition frame rates but, compared to line-by-line acquisition schemes, are very demanding in terms of computational load. This is because, for each transmission, a large image area must be reconstructed instead of a single line. To translate high frame rate applications from academic research to a clinical practice, while maintaining the paramount real-time feedback capability of ultrasound, fast algorithms for image reconstruction are required. At the same time, for an efficient acquisition design, a solid understanding of how the choice of transmission angles influences the image quality is crucial. We, therefore, propose a new physical model for the mathematical description of plane wave acquisitions that leads to a fast, highly parallelizable reconstruction algorithm, provides insights on how image information of different transmit angles is combined during

compounding, and can be used for edge enhancement to increase image quality at high frame rates. In the scope of this contribution, we classify common plane wave reconstruction methods as either delay-and-sum (DAS) based algorithms or Fourier domain (FD) algorithms before we introduce a new class of Radon domain (RD) algorithms.

DAS based methods have in common that the underlying scatter model assumes the scatterer distribution to be composed of a set of point scatterers, which, when excited by an incoming plane wave, create a circular wave field, resulting in a hyperbola-shaped response in the temporal-spatial receive data [see Fig. 1(a)]. Besides pure DAS methods,[2,3] many other beamforming approaches rely on the same wave propagation model. This is the case, for example, for most adaptive beamformers, such as delay-multiply-and-sum methods,[4] short-lag-spatial-coherence methods,[5] or convolutional beamforming methods.[6] While the general DAS algorithm can be applied for all kinds of transmitted wave fronts, some related publications explicitly focus on plane wave acquisitions.[7,8]

In contrast, FD based methods have in common that the underlying scatter model assumes the scatterer distribution to be composed of a set of (plane wave) exponential functions that oscillate monofrequently in one direction and are constant in all perpendicular directions. When these scatterers are excited by an incoming plane wave, the scattered wave field is a monofrequent plane wave, and the respective measurement on a linear array is, again, a (plane wave) exponential function under a different angle [see Fig. 1(b)]. FD based methods include general statements of the Fourier
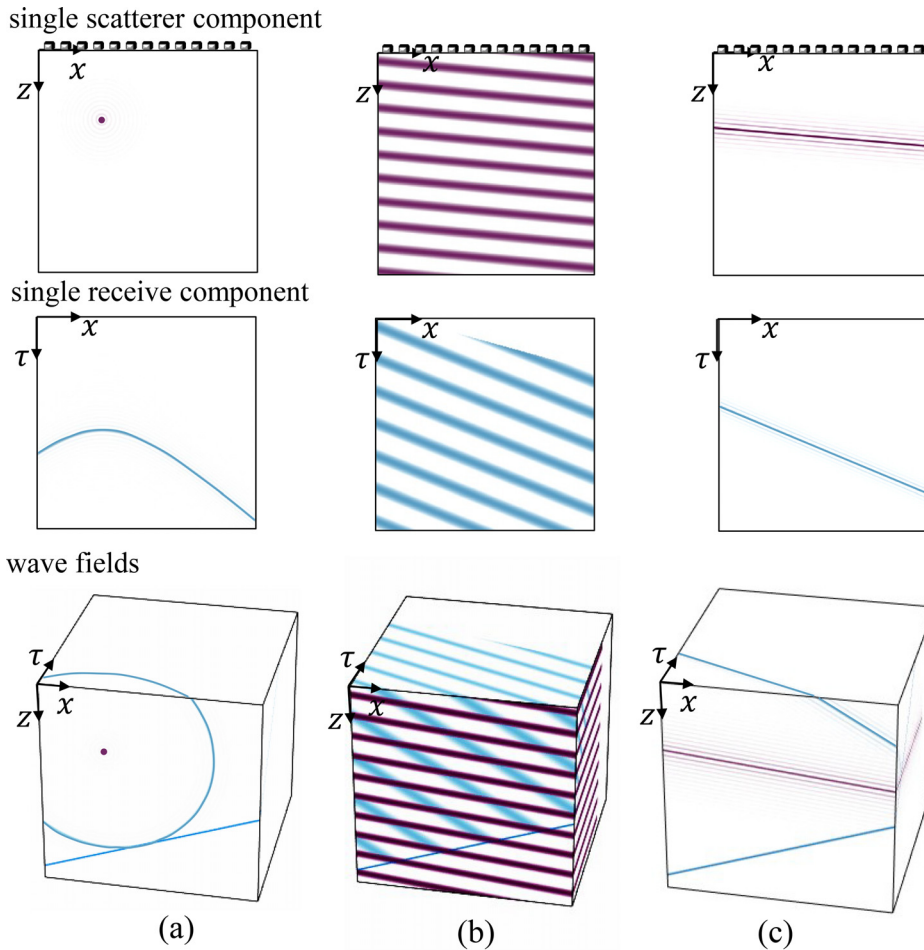
[a])Electronic mail: h.schwab@tue.nl

FIG. 1. (Color online) Illustration of wave field decompositions with the incoming plane wave indicated in dark blue, the single scatterer component in purple, and the scattered wave field in light blue. (a) DAS model for a single point scatterer; (b) FD model for a single monofrequent plane wave scatterer; (c) RD model for a single broadband plane wave scatterer.

(a)   (b)   (c)

diffraction theorem;[9,10] filtered backpropagation,[11] where one of the Fourier transforms is performed on a non-equidistant grid; Fourier slice imaging,[12] which defines the two-dimensional (2D) frequency grid in polar coordinates; and Stolt's migration,[13] which relies on an approximation of the underlying mapping law.

The method proposed in this contribution relies on a scatter model that assumes the scatterer distribution to be composed of filtered lines at a certain depth and under a certain angle. When these line scatterers are excited by an incoming plane wave, they reflect a broadband plane wave. When this broadband plane wave is measured on a linear array transducer, it creates the response of a line in the receive data under a different angle [see Fig. 1(c)]. In Secs. II–IV, the relation between measurement and scatterer distribution in the RD is derived, the performance is compared to DAS and FD methods, and the impact of possible operations in the RD on the image quality is demonstrated. Similar to the spatial FD, which is often related to as "k-space," we abbreviate the RD as "r-space" in the remainder of this paper.

II. THE DIFFRACTION THEOREM

In the following, we derive a RD relation between the scatterer distribution and plane wave receive data. The Radon transform is a linear mapping that transforms a signal defined on spatial coordinates ($\mathbf{r}$) to a signal defined on radial/angular coordinates ($\rho, \mathbf{\Theta}$). We define the Radon transform pair as

$$\mathcal{R}\{p(\mathbf{r})\}(\rho, \mathbf{\Theta}) = \int_{\mathbb{R}^n} p(\mathbf{r})\delta(\mathbf{r} \cdot \mathbf{e}_{\mathbf{\Theta}} - \rho)d\mathbf{r} := \hat{p}(\rho, \mathbf{\Theta}), \quad (1)$$

$$\mathcal{R}^{-1}\{\hat{p}(\rho, \mathbf{\Theta})\}(\mathbf{r}) = \int_{\mathbb{R}}\int_S \hat{p}(\rho, \mathbf{\Theta})h(\mathbf{r} \cdot \mathbf{e}_{\mathbf{\Theta}} - \rho)d\mathbf{\Theta}d\rho, \quad (2)$$

where $\int_S d\mathbf{\Theta}$ is a weighted surface integral and matches $(1/2\pi)\int_0^\pi d\theta$ in two dimensions (Ref. 14, p. 194) and $-(1/8\pi^2)\int_0^{2\pi} d\phi \int_{-\pi/2}^{\pi/2} d\theta \sin(\theta)$ in three dimensions (Ref. 14, p. 328). The function h is the filter function of the filtered back projection and equals $h(\rho) = \partial_\rho \mathcal{H}\delta(\rho)$ in two dimensions and $h(\rho) = \partial_\rho^2 \delta(\rho)$ in three dimensions, with $\mathcal{H}$ being the Hilbert transform operator. The angle vector $\mathbf{\Theta}$ matches θ for two dimensions and (θ, ϕ) in three dimensions, such that the unity vector $\mathbf{e}_{\mathbf{\Theta}}$ is $\mathbf{e}_{\mathbf{\Theta}} = (e_{\mathbf{\Theta}}^{(1)}, e_{\mathbf{\Theta}}^{(2)}) = (\sin(\theta), \cos(\theta))$ in two dimensions and $\mathbf{e}_{\mathbf{\Theta}} = (e_{\mathbf{\Theta}}^{(1)}, e_{\mathbf{\Theta}}^{(2)}, e_{\mathbf{\Theta}}^{(3)}) = (\sin(\theta)\sin(\phi), \sin(\theta)\cos(\phi), \cos(\theta))$ in three dimensions, while $\cdot$ denotes a scalar product. For the sake of compactness, we express the time t in terms of a travel-time equivalent distance $\tau := tc_0$ with the background speed-of-sound c_0.

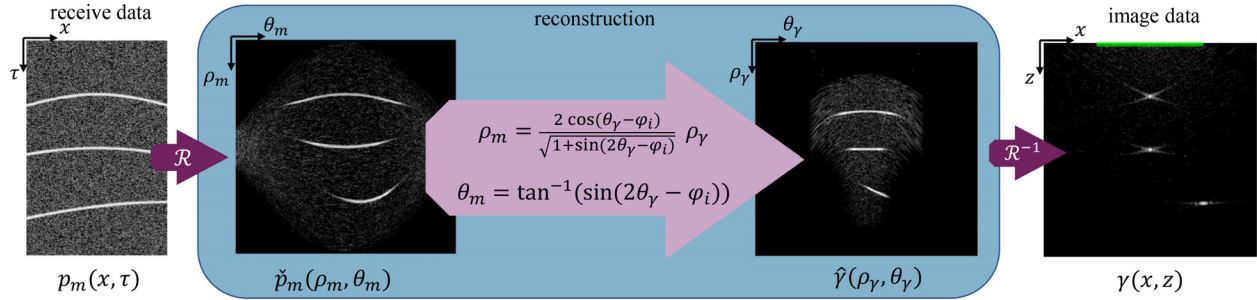In Secs. II A–II C, we derive a mapping law between the arguments of the measurement in the RD $\hat{p}_m(\rho_m, \mathbf{\Theta}_m)$

Hans-Martin Schwab and Richard Lopata

FIG. 2. (Color online) Illustration of RD reconstruction algorithm in two dimensions for a transmitted plane wave under the angle φ_i.

and the arguments of the scatterer distribution in the RD $\hat{\gamma}(\rho_\gamma, \boldsymbol{\Theta}_\gamma)$. Using this relation, a plane wave reconstruction can be performed by a Radon transform of the receive data, followed by an interpolation using the mapping law derived below [see Eqs. (23) and (24)] and the inverse Radon transform. This procedure is depicted in Fig. 2 for the 2D case. A mathematically correct solution also includes the application of a filter function before or after the mapping. The impact of this filter will be assessed in Sec. IV B.

A. A broadband plane wave decomposition

The theorem is based on a decomposition of the wave field into broadband plane waves. In the following, we consider the pressure field $p(\boldsymbol{r}, \tau)$ in an n-dimensional space $\boldsymbol{r} \in \mathbb{R}^n$. All equations hold for $n > 1$. As a preliminary consideration, we transform the n-dimensional homogeneous, isotropic wave equation (Ref. 15, p. 58) into the RD,

$$\mathcal{R}\{(\Delta - \partial_\tau^2)p(\boldsymbol{r}, \tau)\} = 0, \tag{3}$$

$$\int_{\mathbb{R}^n} ((\Delta - \partial_\tau^2)p(\boldsymbol{r}, \tau))\delta(\boldsymbol{r} \cdot \boldsymbol{e}_\Theta - \rho)d\boldsymbol{r} = 0, \tag{4}$$

$$\int_{\mathbb{R}^n} p(\boldsymbol{r}, \tau)(\boldsymbol{e}_\Theta \cdot \boldsymbol{e}_\Theta)\partial_\rho^2\delta(\boldsymbol{r} \cdot \boldsymbol{e}_\Theta - \rho)d\boldsymbol{r}$$
$$- \int_{\mathbb{R}^n} \partial_\tau^2 p(\boldsymbol{r}, \tau)\delta(\boldsymbol{r} \cdot \boldsymbol{e}_\Theta - \rho)d\boldsymbol{r} = 0, \tag{5}$$

$$(\partial_\rho^2 - \partial_\tau^2)\hat{p}(\rho, \boldsymbol{\Theta}, \tau) = 0, \tag{6}$$

where we defined ∂^2 as second order derivative operator and further used $\boldsymbol{e}_\Theta \cdot \boldsymbol{e}_\Theta = 1$. It can immediately be noticed that, in any dimension $n > 1$, the pressure can be expressed as a collection of one-dimensional (1D) wave propagations into different directions $\boldsymbol{\Theta}$. The relation in (6) is the 1D wave equation, which is generally solved by $\hat{p}(\rho, \boldsymbol{\Theta}, \tau) = \hat{p}(\rho \pm \tau, \boldsymbol{\Theta})$ (Ref. 16, p. 4) Hence, any free-field wave propagation can be reduced to a shift of all its Radon coefficients in the radial direction. It also follows that the outgoing free-field Green function in the RD is not a function of $\boldsymbol{\Theta}$ and matches the 1D Green function in the spatial domain (Ref. 16, p. 12),

$$\hat{g}(\rho, \boldsymbol{\Theta}, \tau) = \frac{1}{2}\sigma(\tau - |\rho|), \tag{7}$$

$$= \begin{cases} 0, & \tau < 0 \\ \frac{1}{2}\sigma(\tau - \rho)\sigma(\tau + \rho), & \tau \geqq 0, \end{cases} \tag{8}$$

where $\sigma(\xi)$ is the Heaviside distribution. By applying an inverse Radon transform to $\hat{g}$, we can now express the outgoing (retarded) free-field Green function in space as a decomposition into broadband plane waves $g(\boldsymbol{r}, \tau) := \mathcal{R}^{-1}\hat{g}(\rho, \tau)$,

$$g(\boldsymbol{r}, \tau) = \frac{1}{2}\int_\mathbb{R}\int_S \sigma(\tau - |\rho|)h(\boldsymbol{r} \cdot \boldsymbol{e}_\Theta - \rho)d\rho d\boldsymbol{\Theta}$$
$$= \frac{1}{2}\int_S \mathfrak{h}\delta(\tau - |\boldsymbol{r} \cdot \boldsymbol{e}_\Theta|)d\boldsymbol{\Theta}, \tag{9}$$

where $\mathfrak{h}$ is a filter operator and resembles a convolution with h without one derivative. Using the definition of $\boldsymbol{h}$ and the hull integral in the respective dimensions, we can write the outgoing free-field Green function as $g(\boldsymbol{r}, \tau) = (1/4\pi) \times \int_0^\pi \mathcal{H}_\tau \delta(\tau - |\boldsymbol{r} \cdot \boldsymbol{e}_\theta|)d\theta$ in two dimensions with $\mathcal{H}_\tau$ signifying the Hilbert transform with respect to τ and as $g(\boldsymbol{r}, \tau) = -(1/16\pi^2)\int_{-\pi/2}^{\pi/2}\sin(\theta)\int_0^{2\pi}\delta'(\tau - |\boldsymbol{r} \cdot \boldsymbol{e}_{\theta\phi}|)d\phi d\theta$ in three dimensions with δ' being the first order derivative of the delta distribution. Using this, any wave field that is expressed by means of Green functions can be expressed as a linear combination of broadband plane waves. Apart from the purpose of deriving a reconstruction method, this might also be useful for fast wave field simulations, where the number of considered angles can be used as tuning parameter between accuracy and computation time.

B. The forward problem

For imaging, however, we are interested in a relation between the measurement and the scatterer rather than a relation for the wave field. Therefore, we describe the plane wave measurement $p_m(\boldsymbol{r}^*, \tau)$ with $\boldsymbol{r}^* := (r_1, \ldots, r_{n-1})$ as the wave field at the hyperplane $r_n = 0$, which describes a line sensor in two dimensions and a plane sensor in three dimensions. Instead of performing a Radon transform only in space, we now perform a Radon transform with $n - 1$ spatial dimensions and one temporal dimension, $\check{p}(\rho, \boldsymbol{\Theta}) := \mathcal{R}_{(\boldsymbol{r}^*, \tau)}\{p(\boldsymbol{r}, \tau)\} = \int_{\mathbb{R}^n} p(\boldsymbol{r}^*, r_n, \tau)\delta((\boldsymbol{r}^*, \tau) \cdot \boldsymbol{e}_\theta - \rho)d\boldsymbol{r}^*d\tau$. Applying this to the homogeneous n-dimensional wave equation can, again, be

J. Acoust. Soc. Am. **153** (2), February 2023

Hans-Martin Schwab and Richard Lopata   1017

rewritten in such a way that it is similar to the 1D wave equation as in (6),

$$\mathcal{R}_{(\boldsymbol{r}^*, \tau)}\{(\Delta - \partial_\tau^2)p(\boldsymbol{r}, \tau)\} = 0, \tag{10}$$

$$\mathcal{R}_{(\boldsymbol{r}^*, \tau)}\left\{\left(\left(\partial_\tau^2 - \sum_{i=1}^{n-1}\partial_{r_i}^2\right) - \partial_{r_n}^2\right)p(\boldsymbol{r}, \tau)\right\} = 0, \tag{11}$$

$$\left(w^2\partial_{\rho_m}^2 - \partial_{r_n}^2\right)\check{p}(\rho_m, \boldsymbol{\Theta}_m, r_n) = 0, \tag{12}$$

with ρ_m representing r and r_n representing τ. The only difference from (6) is the factor $w^2 := e_m^{(n)2} - |\boldsymbol{e}_m^*|^2 = 2e_m^{(n)2} - 1$ in front of the second order derivative operator in ρ_m. Since this factor is constant in both ρ_m and r_n, we find that $\check{p}(\rho_m, \boldsymbol{\Theta}_m, r_n) = \check{p}(\rho_m \pm wr_n, \boldsymbol{\Theta})$ solves this differential equation, and, in analogy to the 1D free-field Green function in (7), we can formulate

$$\check{g}(\rho_m, \boldsymbol{\Theta}_m, r_n) = \frac{1}{2}\sigma(-wr_n - \rho_m)|_{r_n\langle 0, \rho_m\rangle 0} \tag{13}$$

as a solution for the Green function in the spatiotemporal RD for $r_n < 0$, which refers to waves traveling into negative r_n direction for $\rho_m > 0$. This covers all waves received at times $\tau > 0$. There are more solutions to $\check{g}$, which refer to waves that propagate away from the sensor or at negative times (see definitions of retarded and advanced Green function in Ref. 16, pp. 6–12). These solutions are ignored here, because they do not play a role in the derivation of the r-space relation in reflection mode. The Green function will now be applied in a convolution to calculate the wave field. Expressing (13) evaluated at the shifted coordinates $\boldsymbol{r} - \boldsymbol{r}'$ and $\tau - \tau'$ and using the shifting property of the Radon transform gives

$$\mathcal{R}_{(\boldsymbol{r}^*, \tau)}\{g(\boldsymbol{r} - \boldsymbol{r}', \tau - \tau')\} = \frac{1}{2}\sigma(-w(r_n - r_n') - \rho_m + (\boldsymbol{r}'^*, \tau')\cdot\boldsymbol{e}_\Theta). \tag{14}$$

This Green function in the spatiotemporal RD is now applied in the calculation of the scattered wave field after insonification by a plane wave.

   We start with the inhomogeneous wave equation, under the assumption that the Born approximation is valid, including compressibility variations $\gamma_\kappa(\boldsymbol{r})$ and mass density variations $\gamma_\rho(\boldsymbol{r})$ as defined in[17]

$$(\Delta - \partial_\tau^2)p_o(\boldsymbol{r}, \tau) = -\gamma_\kappa(\boldsymbol{r})\partial_\tau^2 p_i(\boldsymbol{r}, \tau) + \nabla\cdot\gamma_\rho(\boldsymbol{r})\nabla p_i(\boldsymbol{r}, \tau), \tag{15}$$

where p_i is the incoming (transmitted) wave and p_o is the outgoing (scattered) wave. Note that this wave equation assumes a lossless, isotropic propagation medium. According to the definition of the Green function (Ref. 18, p. 59), this differential equation is solved by $p_o(\boldsymbol{r}, \tau) = -\int_\mathbb{R}\int_\Omega q(\boldsymbol{r}', \tau')g(\boldsymbol{R}, T)d\boldsymbol{r}'d\tau'$, where $q(r, \tau)$ is the right hand side of (15), and $\boldsymbol{R} := \boldsymbol{r} - \boldsymbol{r}'$ and $T := \tau - \tau'$. The spatial integration is defined in the

support region of the source Ω, which is restricted to $r_n > 0$. Under the condition that γ_ρ vanishes at infinity, we can reformulate this convolution as

$$p_o(\boldsymbol{r}, \tau) = +\int_\mathbb{R}\int_\Omega \gamma_\kappa(\boldsymbol{r}')p_i(\boldsymbol{r}', \tau')\partial_{\tau'}^2 g(\boldsymbol{R}, T)d\boldsymbol{r}'d\tau' + \int_\mathbb{R}\int_\Omega \gamma_\rho(\boldsymbol{r}')(\nabla_{\boldsymbol{r}'}p_i(\boldsymbol{r}', \tau')) \times (\nabla_{\boldsymbol{r}'}g(\boldsymbol{R}, T))d\boldsymbol{r}'d\tau', \tag{16}$$

which is similar to the notation in Ref. 11, where the same relation is shown in the temporal frequency domain. We now define an incoming broadband plane wave propagating into the direction defined by $\boldsymbol{e}_i$ as $p_i(\boldsymbol{r}, \tau) = \delta(\boldsymbol{r}\cdot\boldsymbol{e}_i - \tau)$. The amplitude of the plane wave over time and per angle $\hat{p}_i(\tau, \boldsymbol{\Theta}_i)$ is neglected for brevity but can easily be convolved into the final result, since all operations will be linear in τ. By plugging (14) into (17), evaluating the outgoing field at the sensor hyperplane at $r_n = 0$ to get the measurement data $p_m(\boldsymbol{r}^*, \tau) = \int_\mathbb{R}p_o(\boldsymbol{r}, \tau)\delta(r^{(n)})dr^{(n)}$, and then transforming everything into the spatiotemporal RD, we can write

$$\check{p}_m(\rho_m, \boldsymbol{\Theta}_m) = \frac{1}{2}\int_\mathbb{R}\int_\Omega \gamma_\kappa(\boldsymbol{r}')\delta(\boldsymbol{r}'\cdot\boldsymbol{e}_i - \tau') \times \partial_{\tau'}^2\sigma(wr_n' - \rho_m + (\boldsymbol{r}^{*\prime}, \tau')\cdot\boldsymbol{e}_m)d\boldsymbol{r}'d\tau' + \frac{1}{2}\int_\mathbb{R}\int_\Omega \gamma_\kappa(\boldsymbol{r}')(\nabla_{\boldsymbol{r}'}\delta(\boldsymbol{r}'\cdot\boldsymbol{e}_i - \tau')) \times (\nabla_{\boldsymbol{r}'}\sigma(wr_n' - \rho_m + (\boldsymbol{r}^{*\prime}, \tau')\cdot\boldsymbol{e}_m))d\boldsymbol{r}'d\tau' \tag{17}$$

$$= \frac{1}{2}e_m^{(n)2}\int_\Omega \gamma_\kappa(\boldsymbol{r}') \times \delta'\left(\boldsymbol{r}'\cdot\left((\boldsymbol{e}_m^*, w) + e_m^{(n)}\boldsymbol{e}_i\right) - \rho_m\right)d\boldsymbol{r}' + \frac{1}{2}\boldsymbol{e}_i\cdot(\boldsymbol{e}_m^*, w)e_m^{(n)}\int_\Omega \gamma_\rho(\boldsymbol{r}') \times \delta'\left(\boldsymbol{r}'\cdot\left((\boldsymbol{e}_m^*, w) + e_m^{(n)}\boldsymbol{e}_i\right) - \rho_m\right)d\boldsymbol{r}'. \tag{18}$$

Here, we realize the similarity to the Radon transform on the right hand side terms and introduce the scaling, $s := |(\boldsymbol{e}_m^*, w) + e_m^{(n)}\boldsymbol{e}_i| = \sqrt{2}|e_m^{(n)}|\sqrt{1 + \boldsymbol{e}_o\cdot\boldsymbol{e}_i}$, and the unity vector, $\boldsymbol{e}_\gamma := ((\boldsymbol{e}_m^*, w) + e_m^{(n)}\boldsymbol{e}_i)/s = (\boldsymbol{e}_o + \boldsymbol{e}_i)/\sqrt{2 + 2\boldsymbol{e}_o\cdot\boldsymbol{e}_i}$, for which we define the auxiliary unity vector $\boldsymbol{e}_o := (\boldsymbol{e}_m^*, w)/|(\boldsymbol{e}_m^*, w)|$. In doing so, the argument of the δ-distribution becomes $\delta(s\boldsymbol{r}'\cdot\boldsymbol{e}_\gamma - \rho_m) = |s|^{-1}\delta(\boldsymbol{r}'\cdot\boldsymbol{e}_\gamma - \rho_m/s)$, and, hence, the integral matches that of a Radon transform onto a radial coordinate ρ_m that is stretched by s. The choice of the auxiliary unity vector $\boldsymbol{e}_o$ is not completely arbitrary. In fact, there is a descriptive interpretation of the direction $\boldsymbol{e}_o$ is pointing to, which is the direction of broadband plane wave scattered back to the transducer after the incoming plane wave of direction $\boldsymbol{e}_i$ was scattered at a hyperplane with the normal orientation $\boldsymbol{e}_\gamma$. This relation is illustrated in Fig. 3 for the 2D case.

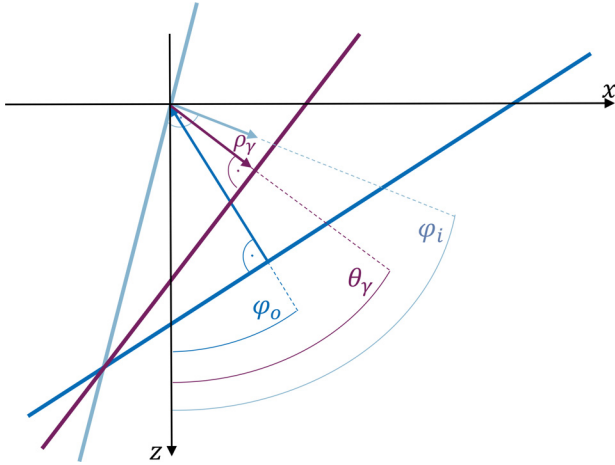Hans-Martin Schwab and Richard Lopata

FIG. 3. (Color online) Illustration of a plane wave scattering event on a line scatterer: The incoming plane wave under the angle φ_i (light blue) is reflected on the line scatterer characterized by the normal angle θ_γ and radial distance ρ_γ (purple), and the reflected wave is a plane wave propagating in negative z direction under the angle $\varphi_o = \sin^{-1}(\tan(\theta_m))$ (dark blue), while the transducer is located at $z = 0$.

We now define the stretched radial component as $\rho_\gamma := \rho_m/s$, and the derivative of the respective δ-distribution becomes $\partial_{\rho m} = |s|^{-1}\partial_{\rho\gamma}$. This relation already describes the mapping law between the radial coordinates of the scatterer and the measurement. The mapping law for the angular coordinate can be expressed in terms of a set of direction cosines $\boldsymbol{e}^* = (e^{(1)}, ..., e^{(n-1)})$, better than in terms of a set of angles $\boldsymbol{\Theta} = (\theta^{(1)}, ..., \theta^{(n-1)})$, which is common practice when working with angles in higher dimensions. We therefore express the angular arguments of $\hat{\gamma}_\kappa$, $\hat{\gamma}_\rho$, and $\check{p}_m$ by their respective direction cosines, which can be bijectively converted to the respective angles (Ref. 19, p. 5). After substituting ρ_γ and $\boldsymbol{e}^*_\gamma$ and some standard algebra, we now get the final relation between measurement and scatterer in the RD,

$$\check{p}_m(\rho_m, \boldsymbol{e}^*_m) = \frac{1}{4(1 + \boldsymbol{e}_o \cdot \boldsymbol{e}_i)} \partial_{\rho\gamma}\hat{\gamma}_\kappa(\rho_\gamma, \boldsymbol{e}^*_\gamma)$$
$$+ \frac{\boldsymbol{e}_o \cdot \boldsymbol{e}_i}{4(1 + \boldsymbol{e}_o \cdot \boldsymbol{e}_i)} \partial_{\rho\gamma}\hat{\gamma}_\rho(\rho_\gamma, \boldsymbol{e}^*_\gamma), \quad (19)$$

with the mapping law,

$$\rho_\gamma = \frac{\rho_m}{|e^{(n)}_m|\sqrt{2 + 2\boldsymbol{e}_o \cdot \boldsymbol{e}_i}}, \quad (20)$$

$$\boldsymbol{e}^*_\gamma = \frac{\boldsymbol{e}^*_o + \boldsymbol{e}^*_i}{\sqrt{2 + 2\boldsymbol{e}_o \cdot \boldsymbol{e}_i}}. \quad (21)$$

The relation is, again, expressed by means of the helper unity vector $\boldsymbol{e}_o$ for brevity, but it can always be expressed as a function of $\boldsymbol{e}_m$ as $\boldsymbol{e}_o = (\boldsymbol{e}^*_m, \sqrt{2 - e^{(n)2}_m})/|e^{(n)}_m|$. The relation holds for $\tau > 0$, which can easily be assumed for a plane wave being transmitted at $\tau = 0$. The derivatives in (19) can be seen as a simple filter term. The relation can be used to design fast, highly parallel pulse-echo simulations.

However, more importantly, it serves as a basis to formulate a solution to the inverse problem that can be used for plane wave reconstruction.

C. The inverse problem

While Eqs. (19)–(21) describe how the measurement can be constructed from given scatterer distributions, we are now interested in describing the scatterer distribution as a function of the receive data. While we can theoretically think of ways to separate the solution for γ_ρ and γ_κ, by solving multiple transmit angles that are mapped onto $\check{p}_m$ at the same locations with different pre-factors in a linear equation system, such approaches are challenging,[20] especially for band limited data and imperfect apertures. It is common practice in ultrasound imaging not to distinguish between the two quantities, but to solve only for a single scatterer distribution, which is the compressibility distribution γ_κ, and to neglect any angle dependent dipole scattering induced by mass density scatterers γ_ρ. Solving (19) for $\hat{\gamma}_\kappa$ gives the inverse solution,

$$\hat{\gamma}_\kappa(\rho_\gamma, \boldsymbol{e}^*_\gamma) = \frac{2\sqrt{2 + 2\boldsymbol{e}_o \cdot \boldsymbol{e}_i}}{e^{(n)}_m} \int_{-\infty}^{\rho m} \check{p}_m(\rho'_m, \boldsymbol{e}^*_m)d\rho'_m, \quad (22)$$

with the mapping law,

$$\rho_m = \frac{\sqrt{2 + 2\boldsymbol{e}_o \cdot \boldsymbol{e}_i}}{\sqrt{1 + |\boldsymbol{e}^*_o|^2}} \rho_\gamma, \quad (23)$$

$$\boldsymbol{e}^*_m = \frac{\boldsymbol{e}^*_o}{\sqrt{1 + |\boldsymbol{e}^*_o|^2}}, \quad (24)$$

where the helper unity vector $\boldsymbol{e}_o$ must now be expressed as a function of $\boldsymbol{e}_\gamma$ and $\boldsymbol{e}_i$ as $\boldsymbol{e}_o = (\boldsymbol{e}_\gamma - \boldsymbol{e}_i)/|\boldsymbol{e}_\gamma - \boldsymbol{e}_i|$, for which we used the fact that $\boldsymbol{e}_\gamma$ is proportional to $\boldsymbol{e}_o + \boldsymbol{e}_i$ and, hence, $\boldsymbol{e}_o$ is proportional to $\boldsymbol{e}_\gamma - \boldsymbol{e}_i$, while its magnitude must be 1. Similar to the derivative in the forward problem (19), here the integration matches a simple filter process. In consequence, in any dimension, a reconstruction can be performed by simple interpolation in the RD, as, after low-pass filtering, each point in the RD of the scatterer matches exactly one point in the RD of the measurement.

1. The solution in two dimensions

In two dimensions, with only one Radon angle, a simple solution for the angle can be formulated, and we do not need to express the angle in terms of its direction cosine. The vector $\boldsymbol{e}^*_\gamma$ in (22) becomes a scalar and matches $\sin(\theta_\gamma)$, with θ_γ being the projection angle of the Radon transform of γ_κ, which is oriented relative to the z axis. The projection angle of the Radon transform of p_m in (22) is defined as θ_m, and the angles of the incoming and outgoing wave are defined as φ_i and φ_o, respectively. From the definition of $\boldsymbol{e}^*_o$ as $\boldsymbol{e}^*_o = \boldsymbol{e}^*_m/|e^{(n)}_m|$, which becomes $\sin(\varphi_o) = \sin(\theta_m)/\cos(\theta_m)$ in two dimensions, it follows that

J. Acoust. Soc. Am. **153** (2), February 2023

Hans-Martin Schwab and Richard Lopata 1019

$$\varphi_o(\theta_m) = \sin^{-1}(\tan(\theta_m)). \quad (25)$$

Likewise, φ_o can be expressed as a function of θ_γ as

$$\varphi_o(\theta_\gamma, \varphi_i) = 2\theta_\gamma - \varphi_i. \quad (26)$$

Expressing (22)–(24) in two dimensions, we can use $e_o \cdot e_i = \cos(\varphi_o - \varphi_i)$, which becomes $\cos(\varphi_o - \varphi_i) = \cos(2(\theta_\gamma - \varphi_i))$ after substituting (26), such that the term $\sqrt{2 + 2\cos(2(\theta_\gamma - \varphi_i))}$ becomes $2\cos(\theta_\gamma - \varphi_i)$ for $|\theta_\gamma - \varphi_i| < \pi/2$, which is always the case for pulse echo. Hence, the solution to the inverse problem expressed without the help of the auxiliary function φ_o reads as

$$\hat{\gamma}_\kappa(\rho_\gamma, \theta_\gamma) = 4\cos(\theta_\gamma - \varphi_i)\sqrt{1 + \sin^2(2\theta_\gamma - \varphi_i)}$$
$$\times \int_0^{\rho m} \check{p}_m(\rho'_m, \theta_m)d\rho'_m \quad (27)$$

with the mapping law

$$\rho_m = \frac{2\cos(\theta_\gamma - \varphi_i)}{\sqrt{1 + \sin^2(2\theta_\gamma - \varphi_i)}}\rho_\gamma, \quad (28)$$

$$\theta_m = \tan^{-1}(\sin(2\theta_\gamma - \varphi_i)). \quad (29)$$

While the entire reconstruction algorithm in two dimensions is depicted in Fig. 2, the mapping law is explicitly illustrated in Fig. 4 for two different plane wave angles. The mapping law exhibits some general properties of a plane wave reconstruction. The region mapped from $\check{p}_m$ is always restricted to the interval $\theta_m \in [-45°, 45°]$, outside of which no data are contained, because these regions refer to evanescent waves. This is because the angle of a plane wave arriving at the transducer line is limited to $|\varphi_o| < 90°$, which, according to (25), refers to a Radon angle of $|\theta_m| < 45°$. We further notice that the measurement data of one plane wave angle φ_i are always mapped onto image data in an interval of $90°$, which is always centered around $\theta_\gamma = \varphi_i$, while the angular resolution decreases the further θ_γ differs from φ_i. The radial resolution of the image data also depends on the angle and is, again, best for $\theta_\gamma = \varphi_i$, while there, the covered radial interval becomes the smallest.

In the frame of this contribution, the r-space plane wave reconstruction was implemented using the Fourier slice theorem (FST) (Ref. 14, p. 166), which states that a Radon transform can be performed by a 1D inverse Fourier transform along radial lines of the 2D spectrum of a data set. Likewise, the inverse Radon transform can be performed by an inverse 2D Fourier transform applied to radially arranged 1D Fourier transforms of Radon projections. It should be noted that the inverse Radon transform only has to be performed once for any number of plane wave angles, because due to the linearity of all operations, compounding can be applied in the RD prior to the inverse transform.

III. RELATION TO OTHER RECONSTRUCTION METHODS

In practice, DAS methods rely on an integration over all sensor elements, while FD methods and RD methods have a one-on-one relation between data points in the FD or RD, respectively. However, it can be shown that all three algorithms rely on the same physical model. In this section, we present how both FD methods and DAS methods relate to the proposed RD methods mathematically. These relations are shown in two dimensions, but the three-dimensional (3D) relations can be derived in a similar fashion.

A. Relation to frequency domain methods

A relation in the FD that is similar to the RD relation in (27) is usually referred to as the Fourier diffraction theorem. It denotes a relation between the measurement in the 2D FD $p_m(k_\tau, k_x)$ and the scatterer distribution in the 2D FD $\gamma(k_z, k_x)$, where $k_\tau = \omega c_0$ is the wave number, k_x is the lateral spatial frequency, and k_z is the axial spatial frequency. The relation reads as[11]

$$p_m(k_\tau, k_x) = \frac{jk_\tau^2}{2\sqrt{k_\tau^2 - k_x^2}}\gamma(k_\tau(e_i + e_o)), \quad (30)$$

where, like before, e_i and e_o are unity vectors pointing into the directions of the incoming (transmitted) and outgoing (received) waves, while here, the direction of the outgoing wave is directly connected to the frequency vector (k_x, k_τ)

(a) $\check{p}_m(\rho_m, \theta_m)$ (b) $\hat{\gamma}(\rho_\gamma, \theta_\gamma)$ for $\varphi_i = 0°$ (c) $\hat{\gamma}(\rho_\gamma, \theta_\gamma)$ for $\varphi_i = 20°$
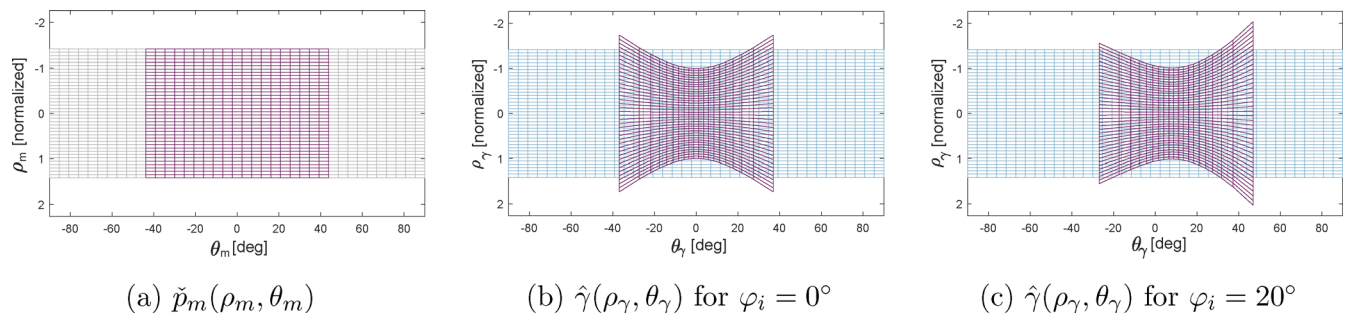
FIG. 4. (Color online) Illustration of the mapping law. The purple region of $\check{p}_m$ in (a) is mapped onto the red area of $\hat{\gamma}$ in (b) and (c), while the transmitted plane wave angle is $\varphi_i = 0°$ in (b) and $\varphi_i = 20°$ in (c).

Hans-Martin Schwab and Richard Lopata

by $e_o = \left(k_x/k_\tau, \sqrt{1-(k_x/k_\tau)^2}\right)$. The equation states that, for each temporal frequency, the lateral frequencies of the receive spectrum are mapped onto a semicircle in the image spectrum with the radius of the respective wave vector, and changes of the angle of the incoming wave rotate the center of that semicircle around the spectrum's origin. Note that in Ref. 11, the orientation of the angles is different from the convention here.

The fact that the FST (Ref. 14, p. 166) states that 2D Fourier data directly relate to Radon data by a radial inverse Fourier transform already hints at the existence of a relation between two quantities in the RD, if a relation in the 2D FD exists. When we express both $p_m(k_t, k_x)$ and $\gamma(k_z, k_x)$ in their respective polar coordinates as $p_m(k_m, \theta_m)$ and $\gamma(k_\gamma, \theta_\gamma)$, we find that the radial frequency vector of γ becomes $k_\gamma = |k_\tau||e_i + e_o| = |k_\tau|\sqrt{2 + 2\cos(\varphi_i - \varphi_o)}$ and that the respective polar angle becomes $\theta_\gamma = \angle(e_i + e_o) = (\varphi_i + \varphi_o)/2$. When we then substitute the mapping law between polar and Cartesian coordinates $k_\tau = k_m \cos(\theta_m)$ and $k_x = k_m \sin(\theta_m)$ into k_γ, θ_γ and the pre-factor in (30), the plane wave Fourier relation in polar coordinates reads as

$$p_m(k_m, \theta_m) = \frac{jk_m \cos(\theta_m)}{2\sqrt{1-\tan^2(\theta_m)}}\gamma(k_\gamma, \theta_\gamma) \tag{31}$$

with the mapping law

$$k_\gamma = \cos(\theta_m)\sqrt{2 + 2\cos(\varphi_i - \varphi_o)}k_m, \tag{32}$$

$$\theta_\gamma = \frac{\varphi_i + \varphi_o}{2}, \tag{33}$$

where we remember that $\varphi_o = \sin^{-1}(\tan(\theta_m))$. This notation in polar coordinates resembles the reconstruction algorithm referred to as Fourier slice imaging.[12] We now apply an inverse Fourier transform to both sides of (31) using the Fourier pair $k_m \leftrightarrow \rho_m$ and perform an integral substitution of k_m by k_γ, as defined in (32), to the right hand side Fourier integral with $dk_m = (1/s)dk_\gamma$, where, as before, $s = |\cos(\theta_m)|\sqrt{2 + 2\cos(\varphi_i - \varphi_o)}$. After the inverse Fourier transform, the term jk_m in the pre-factor becomes a derivative operator ∂_{pm}. This leads to

$$\check{p}_m(\rho_m, \theta_m) = \frac{\cos(\theta_m)}{2s\sqrt{1-\tan^2(\theta_m)}}$$
$$\times \partial_{pm}\hat{\gamma}\left(s\rho_m, \frac{\varphi_i + \sin^{-1}(\tan(\theta_m))}{2}\right). \tag{34}$$

Solving this for $\hat{\gamma}$ and using $|\cos(\theta_m)|/2s\sqrt{1-\tan(\theta_m)^2} = \cos(\theta_m)/2\sqrt{2+2\cos(\varphi_o - \varphi_i)}$ matches exactly the RD relation in (27)–(29).

B. Relation to DAS based methods

In a DAS reconstruction, each pixel is reconstructed by integrating $p_m(\tau, x)$ along a hyperbola in x. The shape of the hyperbola only depends on the distance between pixel and sensor elements, while an additional constant offset for all channels is determined by the travel time of the wavefront to the pixel. For a plane wave measurement, a DAS algorithm is, therefore, usually reported as[2]

$$\gamma(z, x) = \int p_m(\mathbf{r} \cdot \mathbf{e}_i + |(z, x - x')|, x')dx'. \tag{35}$$

An additional delay might be added to the argument of τ to compensate for the time from acquisition start to the time where the plane wave passes the origin of the coordinate system. This equation relies on geometric considerations rather than on a complex wave model, but a relation with great resemblance can be derived from the RD relation. This derivation can be carried out in a similar way, as the filtered back projection can be derived from the FST in computed tomography (Ref. 14, pp. 179–183). By writing down the complete relation in (22), including the Radon transforms, it becomes clear that the order of the two linear operations integration and mapping can be switched,

$$\gamma(\mathbf{r}) = \mathcal{R}^{-1}\{HR\{p_m(\tau, x)\}(\rho_m, \theta_m)\}(z, x) \tag{36}$$

$$= \int\int p_m(\tau, x')M(\mathbf{r}, \tau, x')d\tau\, dx', \tag{37}$$

with $M = \int\int H\delta((\tau, x')\cdot\mathbf{e}_m - \rho_m)\delta(\mathbf{r}\cdot\mathbf{e}_\gamma - \rho_\gamma)d\theta_\gamma d\rho_\gamma$ and H being the filter operator, which is further discussed in Sec. IV B. Substituting the mapping law in (23) and (24) into M, it can be reduced to an integral of the delta distribution $\delta((z, x - x')\cdot\mathbf{e}_{\varphi o} + (z, x)\cdot\mathbf{e}_{\varphi i} - \tau)$ over φ_o. Due to the fact that the term $(z, x - x')\cdot\mathbf{e}_{\varphi o}$ cannot become greater than $|(z, x - x')|$ for any φ_o, M equals 0 for all $\tau > \mathbf{r}\cdot\mathbf{e}_i + |(z, x - x')|$, because the 0 argument of the delta distribution is never reached for any φ_o. This relation exactly matches the τ-argument of p_m in (35). Therefore, (37) can be interpreted as a version of the DAS algorithm in (35) that is filtered in τ, while the filter kernel differs for every reconstructed pixel location (x, z).

IV. VALIDATION

In this section, basic features of the proposed reconstruction method are characterized, and its performance is assessed. In addition, initial feasibility studies for advanced signal processing methods based on the r-space relation are conducted with the aim of image enhancement.

A. The number of projection angles

In contrast to FD mapping and DAS, RD beamforming offers a unique feature, which is the free choice of considered receive angles. This is because, in a discrete Radon transform, the number of projection angles can freely be chosen. Obviously, there is a trade-off between a loss of information if this number is chosen too small and unnecessary computations if the number is too high. In computed tomography, a suggested angular spacing to ensure correct

sampling is reported as $\Delta\theta_m \approx 2\Delta\rho_m/D_m$ (Ref. 14, p. 261f) in radians, where D_m is the diameter of the data set, or largest projection distance, and $\Delta\rho_m$ is the radial spacing. If we assume that $\Delta\rho_m$ matches the temporal spacing $\Delta\tau$, we suggest the number of radial samples $N_\rho = D_m/\rho_m + 1$ to be chosen as $N_\rho = N_t$, which is the number of temporal samples. This means that the suggested angular spacing becomes $\Delta\theta_m \approx 2/N_t$. Unlike in computed tomography, where 180° needs to be covered not to lose any information, for ultrasound receive data, a range of 90° is sufficient, because an angle of $|\theta_m| > 45°$ refers to evanescent waves or, in other words, cannot be received with the aperture, because φ_o is restricted to the interval $[-90°, 90°]$, which restricts $\theta_m = \tan^{-1}(\sin^{-1}(\varphi_o))$ to the interval $[-45°, 45°]$. This leads to a suggested number of projection angles of

$$N_{\theta m} = \frac{\pi}{2} \bigg/ \frac{2}{N_\rho} \approx N_\rho. \tag{38}$$

It is, therefore, considered that, as long as both the number of angular samples and the number of projection angles are on the order of N_t, no information will be lost. To understand whether this number is actually required, or if ultrasound data allow for acceptable image quality for fewer angles, the spatial resolution and the contrast-noise ratio[21] were calculated for an increasing number of projection angles. The analysis was based on the image of a cyst and a wire in the PICMUS data set (Ref. 22). To image the required depth, the number of considered temporal samples was $N_t = 1500$, which was also chosen as the number of radial samples. The results are depicted in Fig. 5 and reveal that image structures can already be recognized at 50 receive angles. Beyond 150 receive angles, the image

quality does not improve significantly anymore, which is only 10% of the theoretically required receive angles in (38). In consequence, the computation time can be vastly reduced without a loss of image quality by choosing a smaller number of projection angles and can be even further reduced if losses in resolution are acceptable. The chosen number of projection angles is, therefore, a simple parameter to tune the trade-off between computation time and image quality.

B. The impact of the filter function

The r-space mapping requires two steps, the interpolation described by the mapping law in (28) and (29) and the filtering described by (27). This section is dedicated to investigating the impact of the filtering step. The filter consists of an angle dependent weighting and radial convolution in the form of an integration. Technically, this r-space filter can be applied either before or after the mapping, depending on whether it is expressed as a function of θ_m or as a function of θ_γ. In (27), the filter is defined after mapping as

$$H(\theta_\gamma, \rho_m) = 4\cos(\theta_\gamma - \varphi_i)\sqrt{1 + \sin(2\theta_\gamma - \varphi_i)^2}$$
$$\times \int_0^{\rho m} d\rho'_m. \tag{39}$$

Since, in ultrasound, receive data are always band limited, the impact of the integration filter, which has an inverse linear transfer function, is expected to be minor. To verify this, the same image was reconstructed with and without application of the r-space filter function. Figure 6 shows the difference in a cross-sectional image of the carotid artery
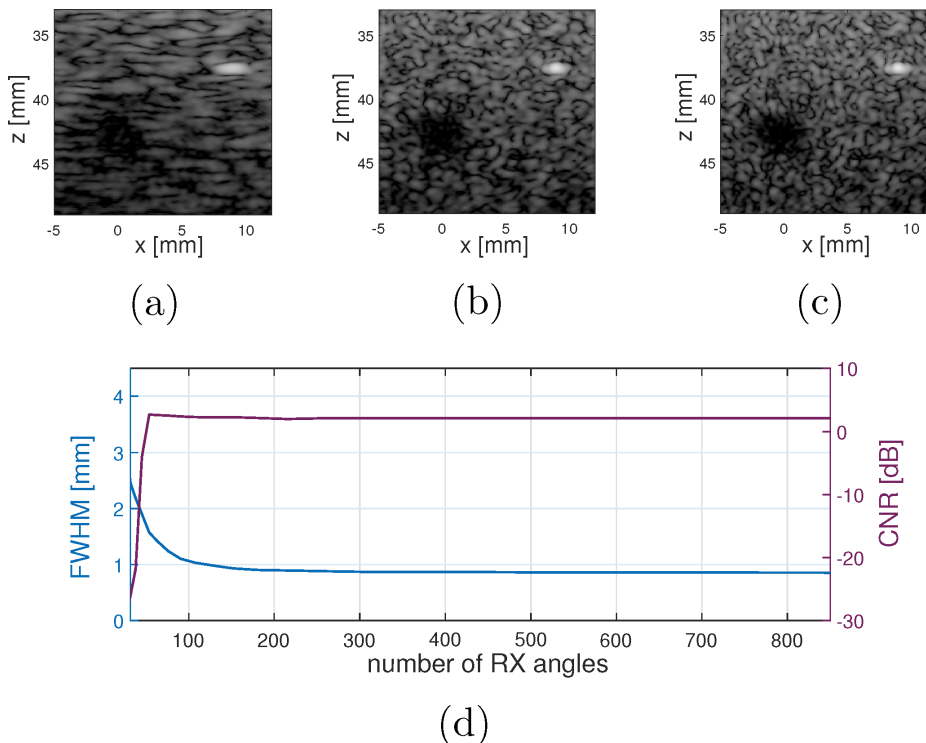

FIG. 5. (Color online) Dependence of image quality on number of considered receive (RX) angles—(a) 50 angles, (b) 150 angles, (c) theoretical minimum 1500 angles, and (d) lateral resolution [quantified by the full width half maximum (FWHM)]—and contrast-to-noise ratio as a function of the number of angles.

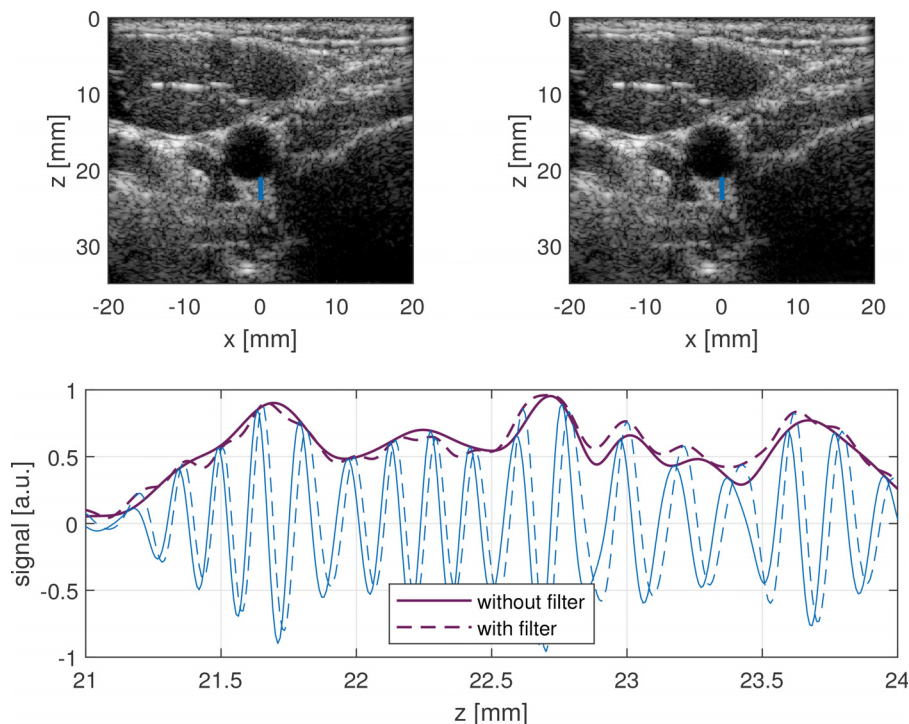Hans-Martin Schwab and Richard Lopata

FIG. 6. (Color online) Impact of r-space filter: image without filter (top left), image with filter (top right). Bottom, line profiles at the indicated location with RF image data (blue) and envelope image data (purple).

from the PICMUS data set.[23] Visually, these differences can barely be seen. Looking at the RF image, the difference energy between the two images is at 75.7% of the single image energy. This error can mostly be explained by the phase shift induced by the integration filter that is also visible in the profiles in Fig. 6. Looking at envelope data, the error reduces to only 1.1% and is, hence, considered to be negligible.

C. Comparison to other reconstruction methods

As pointed out in Sec. III, the Radon based reconstruction method relies on a similar physical model as FD based and DAS based approaches. It can, therefore, be assumed that differences in image quality are dominated in differences in implementation and not in the algorithm itself. To show that our implementation of the r-space reconstruction can return similar results as DAS and FD based methods, the performance with respect to contrast and resolution was compared using the PICMUS plane wave challenge evaluation tool.[22] All reconstructions were performed with an assumed speed-of-sound of 1540 m/s. For a fair comparison of the contrast, the impact of apodization on all three methods is also evaluated. As has been shown, a binary apodization with a fixed F-number relates to a restriction of the receive angle in a FD reconstruction,[23] where the receive angle depends on the frequency vectors by $\varphi_o = \tan^{-1}(k_x/k_t)$. The same concept can be applied to the r-space reconstruction, where the receive angle can directly be derived from the Radon projection angle θ_m as $\varphi_o = \sin^{-1}(\tan(\theta_m))$. The F-number F in a DAS reconstruction relates to the maximum receive angle $\varphi_o^{(max)}$ as $\varphi_o^{(max)} = \tan^{-1}(F/2)$. Figure 7 shows the results of the three reconstruction methods with binary apodization $(F = 1.75, \varphi_o^{(max)} = 16°)$ and without apodization

$(F = 0, \varphi_o^{(max)} = 90°)$, while the analyzed image consists of 11 compounded plane wave angles.

The axial and lateral resolution were compared as -6 dB width of a wire scatterer at 37 mm depth in the PICMUS resolution phantom with binary apodization $(F = 1.75)$. Again, the evaluation was acquired for 11 compounded plane wave angles, as shown in Fig. 8. All results for resolution and contrast are listed in Table I.

Without apodization $(F = 0)$, the contrasts of the FD and the RD reconstruction are much higher than the DAS contrast. This can be explained by the fact that both the FD and RD methods completely neglect evanescent parts
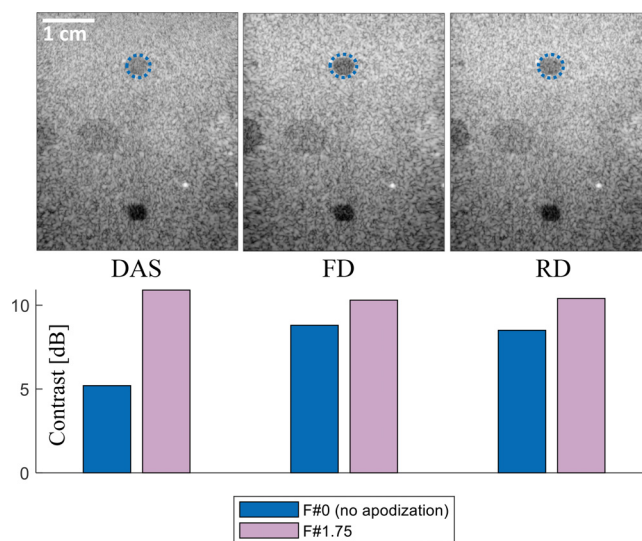

FIG. 7. (Color online) Comparison of the contrast of DAS (left), FD reconstruction (center), and RD reconstruction (right) using the PICMUS contrast tool for 11 plane wave angles at the inclusion indicated by the blue circle.
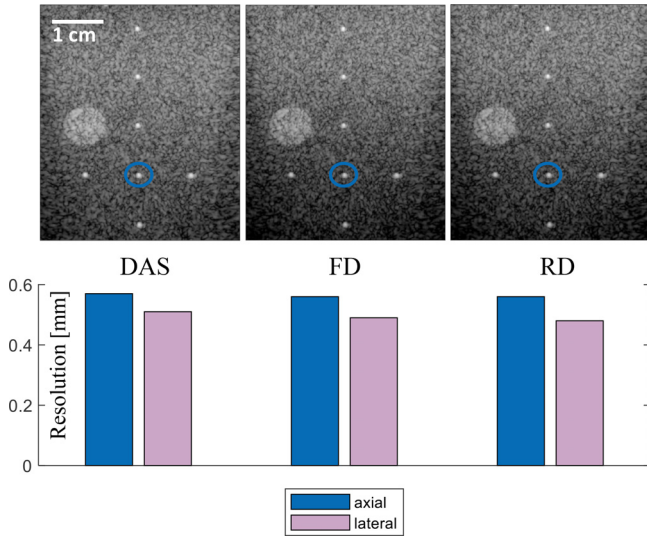
FIG. 8. (Color online) Comparison of the spatial resolution of DAS (left), FD reconstruction (center), and RD reconstruction (right) using the PICMUS resolution and distortion tool for 11 plane wave angles at the wire indicated by the blue circle.

TABLE I. Comparison of reconstruction methods in terms of image quality measures contrast and resolution; all values are for 11 compounded plane wave angles and were evaluated at the locations indicated in Figs. 7 and 8.

	$F=0$ Contrast (dB)	$F=1.75$		
		Contrast (dB)	Axial resolution (mm)	Lateral resolution (mm)
DAS	5.2	10.9	0.57	0.51
FD	8.8	10.3	0.56	0.49
RD	8.5	10.4	0.56	0.48

($|\varphi_o| > 90°$) and, therefore, noise in evanescent parts is automatically automatically cancelled out. However, this benefit is strongly reduced as the F-number increases. Therefore, a general inferiority of DAS cannot be stated. For both lateral and axial resolution, the results of all methods are almost identical, while, again, a slight underperformance of DAS in lateral resolution can be noticed. This might be associated with limitations of a spline interpolation used in the PICMUS reference DAS algorithm. All three algorithms were further assessed in their ability to replicate accurate speckle that follows a Rayleigh distribution using a Kolmogrov–Smirnov test.[22] In the test, all three algorithms performed similarly well, obtaining a significance level of $\alpha = 0.05$.

D. Operations in the Radon domain

In an inverse Radon transform, each value in the RD is back-projected onto a filtered line in the image. Due to the mapping law, each value in the RD representation of the measurement, hence, corresponds to one line in the reconstructed image. A strong image edge will, therefore, lead to a high value at the respective location in the measurement in r-space. This fact can be exploited for edge enhancement by applying any operation that amplifies high values or suppresses low values in r-space. Figure 9 shows a reconstruction of the PICMUS *in vivo* data set, where such an operation was realized as a simple thresholding operation that neglects all values in the measurement in r-space that are lower than -23 dB of the maximum value [Fig. 9(a)]. The comparison to an r-space reconstruction without thresholding exposes an amplification of edges [Figs. 9(b) and 9(c)]. Especially the region labeled by the blue box differs significantly. The reference image exhibits a peak-signal-to-noise ratio (PSNR) of 33.1 dB between vessel wall and upper lumen, where a strong artifact can be noticed at that location, which is likely a reflection artifact. Applying the threshold in r-space suppresses this artifact significantly, leading to a PSNR of 48.1 dB. This implies an artifact suppression of 15.0 dB. In this example, the threshold of -23 dB was chosen manually, but it might be found automatically by an optimization in the future.

Another interesting and important feature of the method lies in the fact that applying this threshold leads to the elimination of most of the values, such that the number of data points after thresholding is only 9% of the data points contained in the original receive data before the Radon transform. Hence, the image in Fig. 9(b) requires only 9% of the
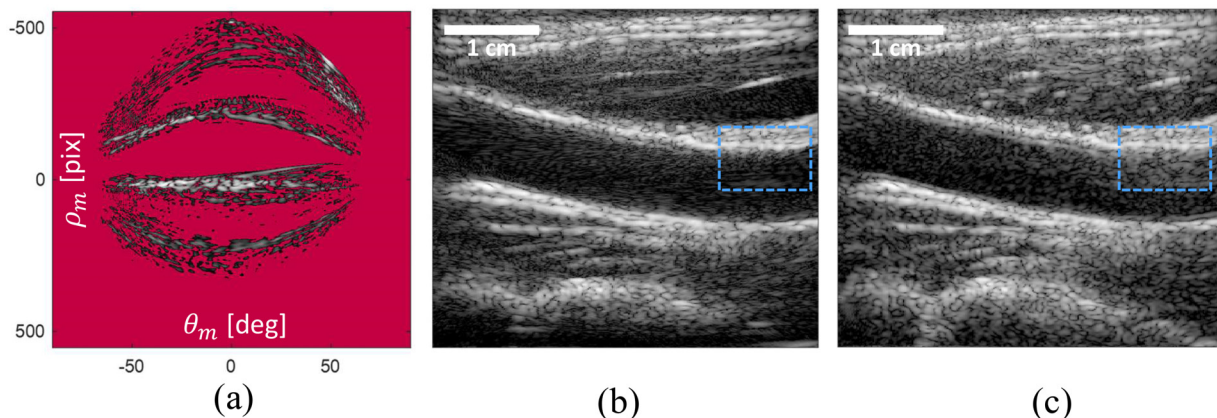

FIG. 9. (Color online) Effect of thresholding in r-space: (a) RD receive data for one receive angle after all values below -23 dB (red mask) were removed, (b) image compounded from 75 receive angles after thresholding in r-space, and (c) reference image without thresholding.

receive data compared to the one in Fig. 9(c), while the image content is maintained or even enhanced in certain regions. This fact offers the potential for data compression in the RD, which might be applied to raw data before beamforming to reduce the amount of data.

V. DISCUSSION AND CONCLUSION

In this contribution, we introduced a novel class of plane wave ultrasound reconstructions, which is based on a mapping law between receive data and image data in the RD. The proposed algorithm is currently restricted to plane wave measurements with linear arrays, but other acquisition types might be converted into these in future studies. This could imply an additional mapping of receive data that synthetically generates plane wave data and then continues with the method as it is proposed here. Just like the other direct reconstruction approaches (DAS and FD), the underlying wave model of our proposed method does not consider an attenuating medium. It can be assumed that a depth dependent attenuation is already partially corrected for using the time variable gain amplifier in ultrasound hardware (Ref. 15, p. 116).

The fact that the proposed method was shown to be based on the same mathematical model as DAS and FD models indicates that differences in performance of these methods might mainly rely on differences in the accuracy of implementation. Differences in the models caused by simplifications in the derivation only lead to different filters that are applied to the data, while, at the same time, it was shown in Sec. IV B that the impact of the filter function on the envelope image was in the range of 1% and can, therefore, be considered negligible in most applications. The hypothesis of comparable performance of the different methods was supported by a comparison of contrast and resolution, where all methods yield similar results, especially if apodization with a fixed F-number is applied.

Huge performance differences, however, might be achieved in terms of computation time.

In terms of computational complexity, DAS has been reported to be $\mathcal{O}(N_t N_e^2)$, while FD methods have been reported to be $\mathcal{O}(N_t N_e \log (N_t N_e))$, with N_t being the number of temporal samples and N_e being the number of channels.[13] In the same line of argumentation, the complexity of RDT would be dominated by the Radon transform and would, therefore, equal $\mathcal{O}(N_t N_e^2)$, just like DAS.[24] However, many efficient solvers for a fast Radon transform have been proposed,[24,25] which offer a great potential compared to DAS based methods. Furthermore, directly computing only the line integrals of Radon coefficients that are required for the image grid can make the mapping step obsolete. The latter approach would resemble the concept of a filtered backpropagation that has been formulated for FD methods.[11]

Compared to FD methods, the limitation of projection angles without a loss in image quality, as pointed out in Sec. IV A, might imply a major computational advantage. Also, while the Fourier transform requires a weighted integration of the data set over all dimensions, the Radon transform

only computes unweighted projections over $n - 1$ dimensions, which, especially for 3D imaging, can improve computation time significantly. The fact that the RD mapping law allows for a 1D interpolation instead of a 2D/3D interpolation can also result in faster implementations compared to FD methods. It should be mentioned that comparisons of computation times were not conducted in this research, as this highly depends on implementation and hardware, and should be investigated in an independent study.

In principle, different reconstruction methods offer the potential for different additional processing steps. While DAS based methods can be easily modified to contain additional temporal and spatial processing steps, and Fourier based methods can be easily modified to contain directional and frequency-related processing steps, our proposed RD method exhibits the potential to be modified for directional, temporal, and, to a certain degree, spatial processing steps. The directional information could, for example, be leveraged for a straightforward integration of medium anisotropy into the model. Further, the fact that each entry in r-space relates to a line in the image might be of importance, as lines or edges, respectively, are understood to be a key factor in visual perception,[26] and structures in band limited images that do not contain absolute gray values are intrinsically constructed of edges rather than areas of constant intensity anyway. This fact has been exploited for edge enhancement and data compression in Sec. IV D. Certainly, the example image of a carotid artery in longitudinal view is strongly dominated by long edges, which might not represent the majority of ultrasound images in general, but still, high values in r-space can be expected for other kinds of coherent object boundaries, while noise and speckle will always exhibit an oscillating behavior along projections and will therefore always result in small values in r-space.

It should be mentioned that applying operations in r-space does not necessarily require a reconstruction in r-space, since the Radon transform might as well be applied to image data in post-processing. However, here, we applied the nonlinear operations before the mapping, which cannot directly be accounted for in post-processing. Also, applying this step during reconstruction can cause a great reduction of computational effort, since only values above the threshold need to be mapped to image data. This could also be leveraged to develop fast methods for data compression of receive data for fast data transfer or efficient data storage. More importantly, approaches for compressed sensing could utilize the sparseness of ultrasound data in r-space, for example, to achieve similar image quality with a reduced number of plane waves. This idea is supported by the fact that Jansen *et al.* showed that optimized compounding weights in the RD always lead to a sparsification.[27] In a similar fashion, deep learning based beamforming approaches might benefit from a representation of data in r-space, where the number of nodes of intermediate layers, for example, in u-nets, could be reduced due to sparsity of ultrasound data.

This reveals new insights of how coherent compounding of different plane wave angles affects the image quality

J. Acoust. Soc. Am. **153** (2), February 2023

Hans-Martin Schwab and Richard Lopata   1025

in terms of angular coverage and directional resolution, which might be used to find optimum choices of plane wave angles or novel strategies for compounding in the future.

In summary, an ultrasound reconstruction class was introduced that offers new possibilities for fast implementation and advanced image quality improvement. Future work will comprise fast hardware accelerated implementations, optimizations of the choice on transmit and receive angles, improved apodization and compounding approaches, and a deeper investigation of compressed sensing methods.

[1]M. Tanter and M. Fink, "Ultrafast imaging in biomedical ultrasound," IEEE Trans. Ultrason. Ferroelectr. Freq. Control 61(1), 102–119 (2014).

[2]G. Montaldo, M. Tanter, J. Bercoff, N. Benech, and M. Fink, "Coherent plane-wave compounding for very high frame rate ultrasonography and transient elastography," IEEE Trans. Ultrason. Ferroelectr. Freq. Control 56(3), 489–506 (2009).

[3]K. E. Thomenius, "Evolution of ultrasound beamformers," in Proceedings of the 1996 IEEE Ultrasonics Symposium, San Antonio, TX (November 3–6, 1996), pp. 1615–1622.

[4]G. Matrone, A. S. Savoia, G. Caliano, and G. Magenes, "The delay multiply and sum beamforming algorithm in ultrasound B-mode medical imaging," IEEE Trans. Med. Imaging 34(4), 940–949 (2015).

[5]M. A. Lediju, G. E. Trahey, B. C. Byram, and J. J. Dahl, "Short-lag spatial coherence of backscattered echoes: Imaging characteristics," IEEE Trans. Ultrason. Ferroelectr. Freq. Control 58(7), 1377–1388 (2011).

[6]R. Cohen and Y. C. Eldar, "Sparse convolutional beamforming for ultrasound imaging," IEEE Trans. Ultrason. Ferroelectr. Freq. Control 65(12), 2390–2406 (2018).

[7]I. K. Holfort, F. Gran, and J. A. Jensen, "Plane wave medical ultrasound imaging using adaptive beamforming," in Proceedings of the 2008 5th IEEE Sensor Array and Multichannel Signal Processing Workshop, Darmstadt, Germany (July 21–23, 2008), pp. 288–292.

[8]G. Chau, R. Lavarello, and J. Dahl, "Short-lag spatial coherence weighted minimum variance beamformer for plane-wave images," in Proceedings of the IEEE International Ultrasonics Symposium, Tours, France (September 18–21, 2016).

[9]A. Devaney, "A filtered backpropagation algorithm for diffraction tomography," Ultrason. Imaging 4, 336–350 (1982).

[10]J. Y. Lu, "2D and 3D high frame rate imaging with limited diffraction beams," IEEE Trans. Ultrason. Ferroelectr. Freq. Control 44(4), 839–856 (1997).

[11]M. F. Schiffner and G. Schmitz, "Plane wave pulse-echo ultrasound diffraction tomography with a fixed linear transducer array," in Acoustical Imaging, edited by A. Nowicki, J. Litniewski, and T. Kujawska (Springer, Dordrecht, Netherlands, 2012).

[12]O. Bernard, M. Zhang, P. Gueth, and J.-P. Thiran, "Ultrasound Fourier slice imaging: A novel approach for ultrafast imaging technique," in Proceedings of the IEEE International Ultrasonics Symposium, Chicago, IL (September 3–6, 2014), pp. 129–132.

[13]D. Garcia, L. L. Tarnec, S. Muth, E. Montagnon, J. Porée, and G. Cloutier, "Stolt's f-k migration for plane wave ultrasound imaging," IEEE Trans. Ultrason. Ferroelectr. Freq. Control 60(9), 1853–1867 (2013).

[14]T. M. Buzug, Computed Tomography, 1st ed. (Springer, Berlin, 2008).

[15]T. L. Szabo, Diagnostic Ultrasound Imaging: Inside Out (Elsevier Academic, New York, 2014).

[16]A. J. Devaney, Mathematical Foundations of Imaging, Tomography and Wavefield Inversion (Cambridge University, Cambridge, UK, 2012).

[17]P. M. Morse and K. U. Ingard, Theoretical Acoustics (McGraw-Hill, New York, 1971).

[18]J. Blackledge, "Electromagnetic scattering solutions for digital signal processing," Ph.D. thesis, University of Jyväskylä, Jyväskylä, Finland, 2010.

[19]J. R. Tyldesley, An Introduction to Tensor Analysis for Engineers and Applied Scientists (Longman, Harlow, UK, 1975).

[20]Q. Barber and R. J. Zemp, "Compressibility and density weighting for ultrasound scattering tomography," IEEE Trans. Ultrason. Ferroelectr. Freq. Control 65(5), 674–683 (2018).

[21]M. S. Patterson and F. S. Foster, "The improvement and quantitative assessment of B-mode images produced by an annular array/cone hybrid," Ultrason. Imaging 5(3), 195–213 (1983).

[22]H. Liebgott, A. Rodriguez-Molares, F. Cervenansky, J. A. Jensen, and O. Bernard, "Plane-wave imaging challenge in medical ultrasound," in Proceedings of the IEEE International Ultrasonics Symposium, Tours, France (September 18–21, 2016).

[23]C. Chen, G. A. G. M. Hendriks, R. J. G. Van Sloun, H. H. G. Hansen, and C. L. De Korte, "Improved plane-wave ultrasound beamforming by incorporating angular weighting and coherent compounding in Fourier domain," IEEE Trans. Ultrason. Ferroelectr. Freq. Control 65(5), 749–765 (2018).

[24]C. Carranza, "Fast and scalable architectures and algorithms for the computation of the forward and inverse discrete periodic Radon transform with applications to 2D convolutions and cross- correlations," Ph.D. thesis, University of New Mexico, Albuquerque, NM, 2016.

[25]D. P. K. Lun, T. C. Hsung, and T. W. Shen, "Orthogonal discrete periodic Radon transform. Part I: Theory and realization," Signal Process. 83(5), 941–955 (2003).

[26]R. M. Shapley and D. J. Tolhurst, "Edge detectors in human vision," J. Physiol. 229, 165–183 (1973).

[27]G. Jansen, N. Awasthi, H. M. Schwab, and R. Lopata, "Enhanced Radon domain beamforming using deep-learning-based plane wave compounding," in Proceedings of the 2021 IEEE International Ultrasonics Symposium (IUS), Xi'an, China (September 11–16, 2021).